

International Journal of Computer Assisted Radiology and Surgery manuscript No.  
(will be inserted by the editor)

# Computer-assisted liver-graft steatosis assessment via learning-based texture analysis

Sara Moccia · Leonardo S. Mattos · Ilaria Patrini · Michela Ruperti ·  
Nicolas Poté · Federica Dondero · François Cauchy · Ailton Sepulveda ·  
Olivier Soubrane · Elena De Momi · Alberto Diaspro · Manuela  
Cesaretti

Received: date / Accepted: date

---

S. Moccia

Department of Advanced Robotics (ADVR), Istituto Italiano di Tecnologia

via Morego 30, 16136 Genoa (GE), Italy

Department of Electronics, Information and Bioengineering (DEIB), Politecnico di Milano

Piazza Leonardo da Vinci, 32, 20133 Milano (MI), Italy

E-mail: sara.moccia@iit.it, sara.moccia@polimi.it

L. S. Mattos

Department of Advanced Robotics (ADVR), Istituto Italiano di Tecnologia

via Morego 30, 16136 Genoa (GE), Italy

I. Patrini

Department of Electronics, Information and Bioengineering (DEIB), Politecnico di Milano

Piazza Leonardo da Vinci, 32, 20133 Milano (MI), Italy

M. Ruperti

Department of Electronics, Information and Bioengineering (DEIB), Politecnico di Milano

Piazza Leonardo da Vinci, 32, 20133 Milano (MI), Italy

Nicolas Poté

Department of Pathology, Hôpital Beaujon, DHU UNITY, AP-HP

Clichy, France

INSERM UMR1149

Paris, France

F. Dondero

Department of HPB Surgery and Liver Transplantation, Hôpital Beaujon, AP-HP

Clichy, France

F. Cauchy

Department of HPB Surgery and Liver Transplantation, Hôpital Beaujon, AP-HP

Clichy, France

A. Sepulveda

Department of HPB Surgery and Liver Transplantation, Hôpital Beaujon, AP-HP

Clichy, France

O. Soubrane

Department of HPB Surgery and Liver Transplantation,

**Abstract Purpose** Fast and accurate graft hepatic-steatosis (HS) assessment is of primary importance for lowering liver-dysfunction risks after transplantation. Histopathological analysis of biopsied liver is the gold-standard for assessing HS, despite being invasive and time consuming. Due to the short time availability between liver procurement and transplantation, surgeons perform HS assessment through clinical evaluation (medical history, blood tests) and liver-texture visual analysis. Despite visual analysis being recognized as challenging in the clinical literature, few efforts have been invested to develop computer-assisted solutions for HS assessment. The objective of this paper is to investigate the automatic analysis of liver texture with machine-learning algorithms to automate the HS assessment process and offer support for the surgeon decision process. **Methods** Forty RGB images of forty different donors were analyzed. The images were captured with an RGB smartphone camera in the operating room (OR). Twenty images refer to livers that were accepted and twenty to discarded livers. Fifteen randomly-selected

---

Hôpital Beaujon, AP-HP

Clichy, France

E. De Momi

Department of Electronics, Information and Bioengineering (DEIB), Politecnico di Milano

Piazza Leonardo da Vinci, 32, 20133 Milano (MI), Italy

A. Diaspro

Department of Nanophysics, Istituto Italiano di Tecnologia via Morego 30, 16136 Genoa (GE), Italy

M. Cesaretti

Department of HPB Surgery and Liver Transplantation, Hôpital Beaujon, AP-HP

Clichy, France Department of Nanophysics, Istituto Italiano di Tecnologia

via Morego 30, 16136 Genoa (GE), Italy

liver patches were extracted from each image. Patch size was  $100 \times 100$ . This way, a balanced dataset of 600 patches was obtained. Intensity-based features ( $INT$ ), histogram of local binary pattern ( $H_{LBP_{riu2}}$ ), and gray-level co-occurrence matrix ( $F_{GLCM}$ ) were investigated. Blood-sample features ( $Blo$ ) were included in the analysis, too. Supervised and semi-supervised learning approaches were investigated for feature classification. The leave-one-patient-out cross-validation was performed to estimate the classification performance. **Results** With the best performing feature set ( $H_{LBP_{riu2}} + INT + Blo$ ) and semi-supervised learning, the achieved classification sensitivity, specificity and accuracy were 95%, 81% and 88%, respectively. **Conclusions** This research represents the first attempt to use machine-learning and automatic texture analysis of RGB images from ubiquitous smartphone cameras for the task of graft HS assessment. The results suggest that is a promising strategy to develop a fully automatic solution to assist surgeons in HS assessment inside the OR.

**Keywords** Liver · Transplantation · Texture analysis · Machine learning · Surgical data science

## 1 Introduction

Liver transplantation (LT) is the treatment of choice for patients with end-stage liver disease for which no alternative therapies are available [4]. Due to increasing demand and shortage in organ supply, expanded donor selection criteria are applied to increase the number of grafts for LT. Since extended criteria donors generates augmented morbidity and mortality in recipient population, liver-graft quality assessment is crucial.

Hepatic steatosis (HS) is one of the most important donor characteristic that can influence graft function and so LT outcome, mostly because of severe ischemia reperfusion injury [13]. Defined as the intracellular accumulation of triglycerides resulting in the formation of lipid vesicles in the hepatocytes, HS is commonly assessed by histopathological examination of liver tissue samples extracted with biopsy. Through visually analyzing the quantities of large sized lipid droplets in the sample, an HS score is assigned to the sample in a semiquantitative fashion. Livers classified as with 5%–30% fatty infiltration are associated with decreased patient and graft survival, but are still considered suitable for transplantation due to the limited donor availability [20]. Severe HS ( $\geq 60\%$ ) is instead associated with primary graft dysfunction or non-function and is not compatible with transplantation [6, 29].

Despite histopathological analysis of biopsied liver tissue being currently the gold reference standard for

diagnosis and grading of HS in liver grafts, it is invasive, time-consuming and expensive. Due to the short time availability between liver procurement and transplantation [24], the surgeon usually performs HS assessment through clinical evaluation (medical history, blood tests) and qualitative visual graft assessment [31]. In this context, visual liver texture analysis is recognized as crucial in grading HS [31]: livers that cannot be transplanted due to high HS (Fig. 1, right) are usually characterized by inhomogeneous texture and are more yellowish than the transplantable ones (Fig. 1, left). It is nonetheless recognized that the precise estimation of HS remains challenging even in experienced hands [31].

On this background, the development of a robust, quantitative, practical, cost-effective and rapid method to support the surgeon in deciding whether to accept or discard liver grafts is mandatory. Considering challenges in diagnosis, preliminary efforts to the automated or semi-automated HS assessment have been proposed and a complete review can be found in [9]. Examples include [28], which reported a sensitivity ( $Se$ ) of 79% in recognizing the HS level from computer-tomography (CT) images, and [19] which reported an area under the receiving operating characteristic curve of 75% by exploiting fibroscanning. Liver-bioelectrical-impedance analysis and Raman spectroscopy were used in [1] and [11], respectively. A semi-automatic HS-grading approach that exploits magnetic resonance (MR) spectroscopy has been proposed in [26], achieving a Spearman correlation coefficient of 0.90.

It is worth noting that all the proposed methodologies require additional imaging instrumentation, which may be not always available in the remote graft-procurement hospitals. Moreover, at most the methods concluded that there is a correlation between liver physical characteristics (e.g., liver stiffness and impedance) and HS grade, without providing a solution for liver-graft quality assessment.

Despite visual liver-texture analysis being crucial for clinical HS assessment [31], to the best of authors' knowledge no efforts have been done to develop a computer-



**Fig. 1** Sample RGB liver images acquired in the operating room. Images are captured with different lighting conditions and different tissue-camera pose. Images refer to a transplanted-liver graft (left) and a discarded one (right).

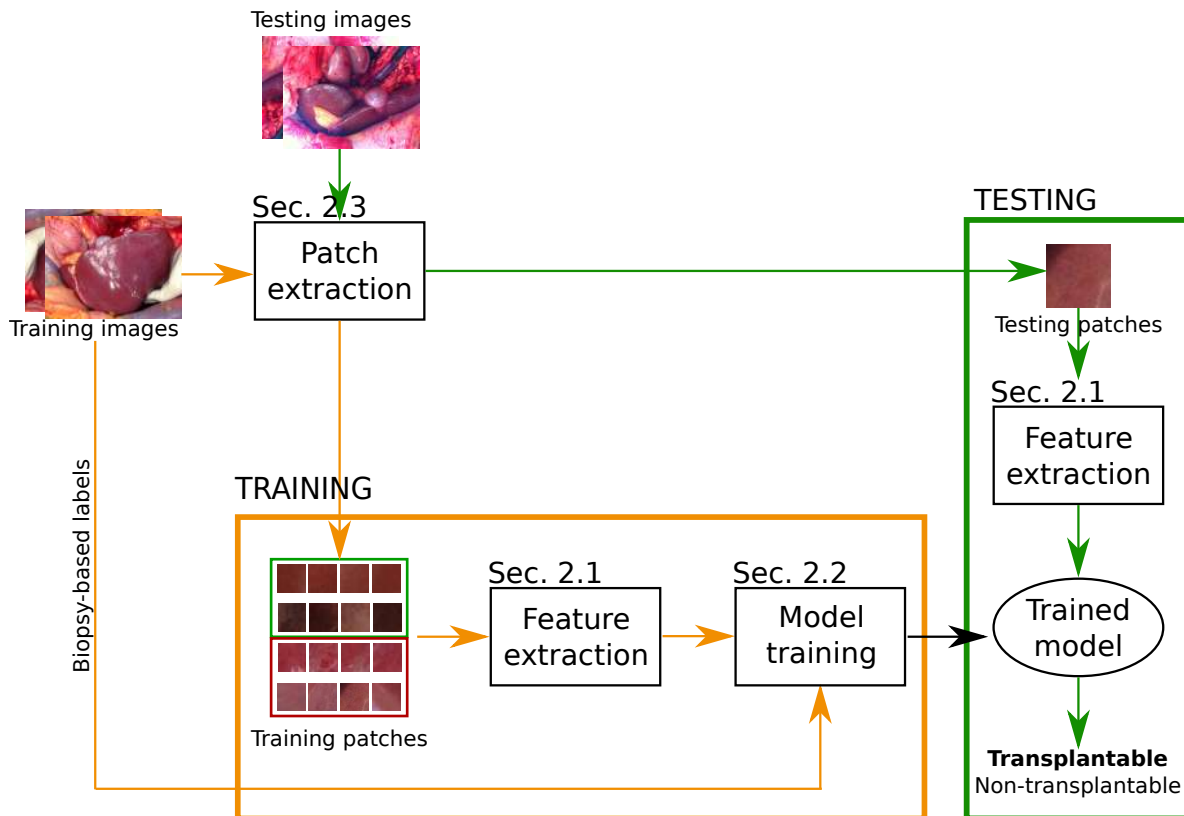


**Fig. 2** . Proposed workflow for graft-hepatic steatosis assessment. From 40 RGB liver images of 40 different donors, a dataset of patches with size  $100 \times 100$  is extracted. From each patch, a set of textural features is computed. The dataset is divided in training and testing patches. The features from the training patches are used to train a classifier model. The trained model is used to assess HS from the testing patches.

assisted diagnostic tool that exploits automatic texture analysis to assess graft steatosis. Moreover, liver texture analysis has the advantage of being performed on standard RGB optical imaging, without requiring additional instrumentations. It is worth noting that modern cellphone cameras provide decent quality images for liver assessment and are ubiquitous. Therefore, they could be the solution for automatic HS assessment not only in remote hospitals, but also in low-income countries where other imaging equipment may not be available. Indeed, the use of RGB cameras for tissue classification is becoming quite popular in different fields, such as skin-cancer diagnosis [8].

The emerging and rich literature on surgical data science for tissue classification in optical images outside the field of HS assessment is focusing more and more on using machine-learning algorithms to classify tissues according to texture-based information [18]. The histogram of local binary patterns (LBP) is exploited for tissue classification in several anatomical districts, such as abdomen, larynx, gastro-intestinal tract (e.g. [15, 32, 23, 22, 16]). Gray-level co-occurrence matrix (GLCM)-based features have also been exploited for tis-

sue classification. Examples include [30] for gastroscopy and [21] for colorectal images.

Inspired by these recent and promising studies, and in particular by our previous research focused on the laryngeal district [22], in this paper we aim at investigating if liver-texture analysis from RGB images acquired with smartphones in the operating room (OR) coupled with machine learning can provide reliable results, to be used as support for LT decision.

This paper is organized as follows: Sec. 2 explains the proposed approach to textural feature extraction and classification. The results are presented in Sec. 3 and discussed in Sec. 4, reporting the main strengths and drawback of the proposed approach and suggesting future work to overcome the drawbacks. To conclude, 5 summarizes the contribution of this paper.

## 2 Methods

In this section, the feature extraction strategy is explained (Sec. 2.1) as well as the classification-model training (Sec. 2.2). We will explore both supervised (Sec. 2.2.1) and semi-supervised (Sec. 2.2.2) classifi-

cation approaches. The evaluation protocol, which includes materials, parameter setting and performance-measure definition, is explained in Sec. 2.3. The workflow of the proposed method for LT assessment is shown in Fig. 2.

## 2.1 Feature extraction

When choosing the classification features, it is necessary to consider that liver images may be captured under various illumination conditions and from different viewpoints. As a consequence, the features should be robust to the camera pose as well as to the lighting conditions. Furthermore, with a view of a real-time computer-aided application, they should be computationally cheap. LBPs fully meet these requirements [25].

A rather popular LBP formulation is the uniform rotation-invariant one ( $LBP_{riu2}^{R,P}$ ). The  $LBP_{riu2}^{R,P}$  formulation requires to define, for a pixel  $\mathbf{c} = (c_x, c_y)$ , a spatial circular neighborhood of radius  $R$  with  $P$  equally-spaced neighbor points ( $\{\mathbf{p}_p\}_{p \in (0, P-1)}$ ):

$$LBP_{riu2}^{R,P}(\mathbf{c}) = \begin{cases} \sum_{p=0}^{P-1} s(g_{\mathbf{p}_p} - g_{\mathbf{c}}), & \text{if } U(LBP^{R,P}) \leq 2 \\ P + 1, & \text{otherwise} \end{cases} \quad (1)$$

where  $g_{\mathbf{c}}$  and  $g_{\mathbf{p}_p}$  denote the gray values of the pixel  $\mathbf{c}$  and of its  $p^{th}$  neighbor  $\mathbf{p}_p$ , respectively.  $s(g_{\mathbf{p}_p} - g_{\mathbf{c}})$  is defined as:

$$s(g_{\mathbf{p}_p} - g_{\mathbf{c}}) = \begin{cases} 1, & g_{\mathbf{p}_p} \geq g_{\mathbf{c}} \\ 0, & g_{\mathbf{p}_p} < g_{\mathbf{c}} \end{cases} \quad (2)$$

and  $U(LBP^{R,P})$  is defined as:

$$U(LBP^{R,P}) = |s(g_{\mathbf{p}_{P-1}} - g_{\mathbf{c}}) - s(g_{\mathbf{p}_0} - g_{\mathbf{c}})| + \sum_{p=1}^{P-1} |s(g_{\mathbf{p}_p} - g_{\mathbf{c}}) - s(g_{\mathbf{p}_{p-1}} - g_{\mathbf{c}})| \quad (3)$$

Here, the  $H_{LBP_{riu2}^{R,P}}$ , which counts the occurrences of  $LBP_{riu2}^{R,P}$ , was used as textural feature and normalized to the unit length.

To include image intensity information, which has been reported as related to the HS level from the clinical community [31], we also included intensity-based features ( $INT$ ), which consisted of image mean and standard deviation, computed for each RGB channel in the image.

For comparison, we also extracted the GLCM matrix-based textural features. The GLCM computes how often pair of pixels ( $\mathbf{c}, \mathbf{q}$ ) with specific values and in a specified spatial relationship (defined by  $\theta$  and  $d$ , which

are the angle and distance between  $\mathbf{c}$  and  $\mathbf{q}$ ) occur in an image. In the GLCM formulation, the GLCM width ( $W$ ) is equal to the GLCM height ( $H$ ) and corresponds to the number of quantized image intensity gray-levels. For the  $w = h$  intensity gray-level, the GLCM computed with  $\theta$  and  $d$  is defined as:

$$GLCM_{\theta,d}(h, w) = \begin{cases} 1, & I(\mathbf{c}) = h \text{ and} \\ & I(c_x + d \cdot \cos(\theta), c_y + d \cdot \sin(\theta)) = w \\ 1, & I(\mathbf{c}) = h \text{ and} \\ & I(c_x - d \cdot \cos(\theta), c_y - d \cdot \sin(\theta)) = w \\ 0, & \text{otherwise} \end{cases} \quad (4)$$

We extracted GLCM-based features from the normalized  $GLCM_{\theta,d}$ , which expresses the probability of gray-level occurrences, is obtained by dividing each entry of the  $GLCM_{\theta,d}$  by the sum of all entries, as suggested in 10. The GLCM feature set ( $F_{GLCM}$ ) consisted of GLCM contrast, correlation, energy and homogeneity.

As in [22], and since texture is a local image-property, we decided to compute textural features from image patches, which were extracted as explained in Sec. 2.3.

## 2.2 Model training

In this section, we will first describe our approach for supervised patch classification (Sec. 2.2.1). In Sec. 2.2.2 we will deal with the semi-supervised approach for image classification.

### 2.2.1 Supervised approaches for patch classification

To perform patch classification, support vector machines (SVM) with the Gaussian kernel ( $\Psi$ ) were used [3]. Indeed, SVM allowed overcoming the *curse-of-dimensionality* that arises analyzing our high-dimensional feature space [5, 17]. The *kernel-trick* prevented parameter proliferation, lowering computational complexity and limiting over-fitting. Moreover, as the SVM decisions are only determined by the support vectors, SVM are robust to noise in training data. For our binary classification problem, given a training set  $T = \{y_t, \mathbf{x}_t\}_{t \in T}$ , where  $\mathbf{x}_t$  is the  $t^{th}$  input feature vector and  $y_t$  is the  $t^{th}$  output label, the SVM decision function ( $f$ ), according to the ‘‘dual’’ SVM formulation, takes the form of:

$$f(\mathbf{x}) = \text{sign} \left[ \sum_{t \in T} a_t^* y_t \Psi(\mathbf{x}, \mathbf{x}_t) + b \right] \quad (5)$$

where:

$$\Psi(\mathbf{x}, \mathbf{x}_t) = \exp\{-\gamma\|\mathbf{x} - \mathbf{x}_t\|_2^2/\sigma^2\}, \quad \gamma > 0 \quad (6)$$

$b$  is a real constant and  $a_t^*$  is computed as follow:

$$a_t^* = \max \left\{ -\frac{1}{2} \sum_{k,l=1}^N y_t y_l \Psi(\mathbf{x}_t, \mathbf{x}_l) a_t a_l + \sum_{t \in \mathbf{T}} a_t \right\} \quad (7)$$

with:

$$\sum_{t \in \mathbf{T}} a_t y_t = 0, \quad 0 \leq a_t \leq C, \quad t \in \mathbf{T} \quad (8)$$

In this paper,  $\gamma$  and  $C$  were retrieved with grid search and cross-validation on the training set, as explained in Sec. 2.3.

For the sake of completeness, the performance of random forest (RF) [2] in classifying image patches was also investigated.

### 2.2.2 Semi-supervised approach for image classification

After performing the patch classification with SVM and RF, we identified the best-performing feature set as the one that guarantees the highest *Se*. With the best-performing feature set, we further investigated the use of multiple instance learning (MIL), a semi-supervised machine-learning technique, for performing full image classification (instead of patch classification) from patch-based features. In fact, it is worth noting that the pathologist gold-standard biopsy-based classification is associated to the whole image, and not to the single patch. Thus, considering all patches from an image of a graft with high HS as pathological may influence the classification outcome, as HS is commonly not homogeneous in the hepatic tissue [31]. Therefore, we decided to investigate if MIL can support HS diagnosis from (unlabeled) patches extracted from (labeled) RGB images.

Among MIL algorithms, we investigated the use of single instance learning (SIL) [27], which has the strong advantage of allowing the fusion of patch-wise information (such as textural features) with image-wise information (such as blood-sample features) [27], thus providing further information for the classification process. Here, we decided to investigate the popular SVM-SIL formulation, which showed good classification performance in several fields outside the proposed one [27].

For our semi-supervised binary classification problem, let  $\mathbf{T}_p \subseteq \mathbf{T}$  be the set of positive images (rejected grafts), and  $\mathbf{T}_n \subseteq \mathbf{T}$  the set of negative images (accepted grafts). Let  $\tilde{\mathbf{T}}_p = \{t \mid t \in \mathbf{T}_p\}$  and  $\tilde{\mathbf{T}}_n = \{t \mid t \in \mathbf{T}_n\}$  be the patches from positive and negative images, respectively. Let  $L = L_p + L_n = |\tilde{\mathbf{T}}_p| + |\tilde{\mathbf{T}}_n|$  be the total number of patches. For any patch  $t \in \mathbf{T}$



**Fig. 3** Dataset sample images. The images refer to (first row) accepted and (second row) rejected liver grafts. Images were acquired at different distance and orientation with respect to the liver. Images present different illumination levels. Specular reflections are present due to the smooth and wet liver surface.

from an image  $T \in \mathbf{T}$ , let  $\mathbf{x}_t$  be the feature vector representation of  $t$ . Thus,  $\mathbf{x}_T = \sum_{t \in T} \mathbf{x}_t$  is the feature vector representation of image  $T$ . The SVM-SIL optimization, here written in the “primal” SVM formulation for better readability, aims at minimizing  $\mathbf{J}$ :

$$\mathbf{J}(\mathbf{w}, b, \xi) = \frac{1}{2} \|\mathbf{w}\|^2 + \frac{C}{L} \sum_{X \in \mathcal{X}} \sum_{x \in X} \xi_x \quad (9)$$

subject to:

$$\mathbf{w}\mathbf{x}_t + b \leq -1 + \xi_t, \quad \forall t \in \tilde{\mathbf{T}}_n \quad (10)$$

$$\mathbf{w}\mathbf{x}_t + b \geq +1 - \xi_t, \quad \forall t \in \tilde{\mathbf{T}}_p \quad (11)$$

$$\xi_t \geq 0 \quad (12)$$

where  $\xi_t$  is the relaxing term introduced for the soft-margin SVM formulation,  $b$  is a real value,  $\mathbf{w}$  the SVM weight vector. Also in this case,  $C$  was retrieved with grid search and cross-validation on the training set, as explained in Sec. 2.3.

As SIL allows fusing patch-wise (i.e. texture features) and image-wise (i.e. blood features) features, in addition to the best-performing feature set, features from blood tests (*Blo*) were used, too. In particular, alanine aminotransferase, aspartate aminotransferase, bilirubin, liver Hounsfield unit (HU), difference between the liver and the spleen HU, and gamma glutamyl transferase were considered. Further, patient’ age, weight and height were also considered. Thus, *Blo* feature size was 9. The *Blo* features are commonly used for HS assessment by surgeons [31], as introduced in Sec. 1. Thus, their use would not alter the actual clinical practice.

## 2.3 Evaluation

In this study, we analyzed 40 RGB images, which refer to 40 different potential liver donors. HS was assessed with histopathological analysis performed after liver biopsy.



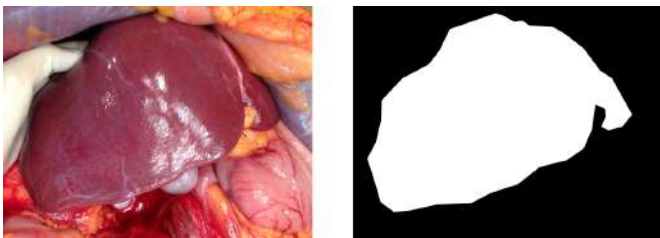


**Fig. 4** Liver and liver mask obtained through manual segmentation

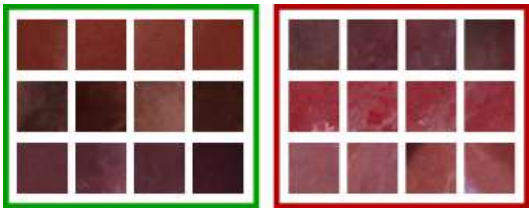


**Fig. 5** Dataset sample patches. The green and red boxes refer to patches extracted from transplanted and non-transplanted livers. Each row in a box refers to patches extracted from the same liver image.

Biopsy was performed during procurement, taking surgical triangular hepatic samples up to 2 cm. One pathologist analyzed the histological sections. Steatosis was visually assessed based on the percentage of hepatocytes with intracellular large lipid droplets by using a semi-continuous scale [0%:5%:100%].

From the dataset, 20 livers referred to discarded grafts, as with a HS  $\geq 60\%$ . The remaining 20 livers had a HS  $\leq 20\%$  and were transplanted. Images were acquired with a smartphone RGB camera. Image size was  $1920 \times 1072$  pixels. All the images were acquired with open-surgery view, as no laparoscopic procurement is performed for cadaveric donors [14]. Challenges associated with the dataset included:

- Wide range of illumination
- Varying camera pose
- Presence of specular reflections
- Different organ position

Visual samples of liver images are shown in Fig. 3.

From each image, liver manual segmentation was performed to separate the hepatic tissue from the background (Fig. 4). The manual segmentation of the liver images was performed with the help of the software Matlab <sup>®</sup>. The liver contour in each image was manually drawn by marking seed points along the liver edges, which were then connected with straight lines by the software.

The whole image was then divided in non-overlapping patches of size  $100 \times 100$  pixels starting from the top-left image corner. We chose such patch size as image-patch size is usually of the order of magnitude of  $10^2 \times 10^2$  pixels (e.g. [32]). The rightmost part of the image, for which

it was not possible to select full patches, was discarded. This did not represent a problem since the liver was always displayed at the center of the image. A patch was considered valid for our analysis if it overlapped with at least 90% of the liver mask.

To have the same number of patches from each patient, we first computed the minimum number of image patches that we could obtain among all images, which was 15. Then, we randomly extracted 15 patches from all the other images. As result, our patch dataset was composed of 300 patches extracted from transplanted liver and 300 from non-transplanted ones. Sample patches for transplanted and non-transplanted livers are shown in Fig. 5.

For the feature extraction described in Sec. 2.1, the  $LBP_{R,P}^{riu2}$  were computed with the following  $(R;P)$  combinations: (1;8), (2;16), (3;24), and the corresponding  $H_{LBP_{riu2}}$  were concatenated. Such choice allows a multi-scale, and therefore a more accurate description of the texture, as suggested in [22]. The  $LBP_{R,P}^{riu2}$  were computed for each RGB image channel.

Nine  $GLCM_{\theta,d}$  were computed for each RGB channel using all the possible combinations of  $(\theta, d)$ , with  $\theta \in \{0^\circ, 45^\circ, 90^\circ\}$  and  $d \in \{1, 2, 3\}$ , and the corresponding  $F_{GLCM}$  sets were concatenated. The chosen interval of  $\theta$  allows to approximate rotation invariance, as suggested in [10]. The values of  $d$  were chosen to be consistent with the scale used to compute  $LBP_{R,P}^{riu2}$ .

Prior to classification, we also investigated feature reduction by means of principal component analysis (PCA). In particular, we applied PCA on our best-performing (highest  $Se$ ) feature set. We then retained the first principal components with explained variance equal to 98% and performed the classification described in Sec. 2.2.1.

For performing the classification presented in Sec. 2.2, the SVM hyper-parameters, for both the supervised and semi-supervised approaches, were retrieved via grid-search and cross-validation on the training set. The grid-search space for  $\gamma$  and  $C$  was set to  $[10^{-10}, 10^{-1}]$  and  $[10^0, 10^{10}]$ , respectively, with 10 values spaced evenly on  $\log_{10}$  scale in both cases. The number of trees for RF training was retrieved with a grid-search space set to  $[40, 100]$  with six values spaced evenly.

The feature extraction and classification were implemented with scikit-image<sup>1</sup> and scikit-learn<sup>2</sup>.

We evaluated the classification performance of SVM, RF and SVM-SIL using leave-one-patient-out cross validation. Each time, the patches extracted from one patient were used for testing the performance of the classification model (SVM, RF or SVM-SIL) trained with

<sup>1</sup> <http://scikit-image.org/>

<sup>2</sup> <http://scikit-learn.org>

**Table 1** Tested feature vectors for supervised patch classification with support vector machines and random forest and corresponding number of features. *INT*: Intensity mean and variance; *FGLCM*: Gray-level co-occurrence matrix-based descriptors; *H<sub>LBP<sub>riu2</sub></sub>*: Normalized histogram of rotation-invariant uniform local binary patterns.

Feature vector	<i>INT</i>	<i>FGLCM</i>	<i>H<sub>LBP<sub>riu2</sub></sub></i>	<i>H<sub>LBP<sub>riu2</sub></sub></i> + <i>INT</i>
Number of features	6	108	162	168

**Table 2** Area under the receiving operating characteristic (ROC) curve obtained with support vector machines (SVM) and different feature vectors. *INT*: intensity mean and variance; *FGLCM*: Gray-level co-occurrence matrix-based descriptors; *H<sub>LBP<sub>riu2</sub></sub>*: Normalized histogram of rotation-invariant uniform local binary patterns.

	Area under the ROC
<i>INT</i>	0.65
<i>FGLCM</i>	0.71
<i>H<sub>LBP<sub>riu2</sub></sub></i> + <i>INT</i>	0.76
<i>H<sub>LBP<sub>riu2</sub></sub></i>	0.77

**Table 3** Patch-classification performance measure obtained with support vector machines (SVM) and different feature vectors. *INT*: Intensity mean and variance; *FGLCM*: Gray-level co-occurrence matrix-based descriptors; *H<sub>LBP<sub>riu2</sub></sub>*: Normalized histogram of rotation-invariant uniform local binary patterns. *Se* = Sensitivity; *Sp* = Specificity, *Acc* = Accuracy.

	<i>Se</i>	<i>Sp</i>	<i>Acc</i>
<i>INT</i>	0.58	0.80	0.69
<i>FGLCM</i>	0.73	0.60	0.66
<i>H<sub>LBP<sub>riu2</sub></sub></i> + <i>INT</i>	0.80	0.64	0.72
<i>H<sub>LBP<sub>riu2</sub></sub></i>	0.82	0.64	0.73

(only) the images of all the remaining patients. The separation at patient level was necessary to prevent data leakage.

To evaluate the classification performance, we computed the classification *Se*, specificity (*Sp*) and accuracy (*Acc*), where:

$$Se = \frac{TP}{TP + FN} \quad (13)$$

$$Sp = \frac{TN}{TN + FP} \quad (14)$$

$$Acc = \frac{TP + TN}{TN + FP + TP + FN} \quad (15)$$

being *TP*, *TN*, *FP* and *FN* the number of true positive, true negative, false positive and false negative, respectively.

We used the Wilcoxon signed-rank test (significance level  $\alpha = 0.05$ ) for paired sample to assess whether the classification achieved with our best-performing (highest *Se*) feature vector significantly differs from the ones achieved with the other feature sets in Table 1.

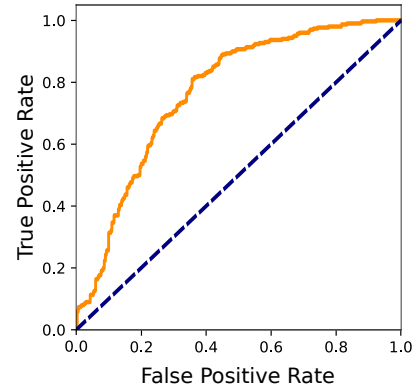


**Fig. 6** Receiving operating characteristic (ROC) curve for classification with the normalized histogram of rotation-invariant uniform local binary patterns and support vector machines.

**Table 4** Patch-classification performance measure obtained using the histogram of rotation-invariant local binary patterns as feature with different classifiers. Classification with feature reduction is reported, too. *Se* = Sensitivity; *Sp* = Specificity, *Acc* = Accuracy; PCA: Principal component analysis, SVM = Support vector machines, RF = Random forest.

	<i>Se</i>	<i>Sp</i>	<i>Acc</i>
SVM + PCA	0.83	0.62	0.73
RF	0.72	0.61	0.67
SVM	0.82	0.64	0.73

### 3 Results

Table 2 shows the area under the ROC for the SVM classification obtained with the feature vectors in Table 1. The higher area under the ROC (0.77) was obtained with *H<sub>LBP<sub>riu2</sub></sub>*. The relative ROC curve is shown in Fig. 6.

The classification performance obtained with SVM and *INT*, *FGLCM*, *H<sub>LBP<sub>riu2</sub></sub>* and *H<sub>LBP<sub>riu2</sub></sub>* + *INT* are shown in Table 3. The best performance was obtained with *H<sub>LBP<sub>riu2</sub></sub>*, with *Se* = 0.82, *Sp* = 0.64 and *Acc* = 0.73. Using only *INT* features led to the worst classification performance for rejected grafts with *Se* = 0.58. Significant differences were found when comparing our best performing feature (*H<sub>LBP<sub>riu2</sub></sub>*) with *INT* and *FGLCM*. The confusion matrices for feature comparison are reported in Fig. 7.

When exploiting PCA-based feature reduction for *H<sub>LBP<sub>riu2</sub></sub>*, *Se* = 0.83, *Sp* = 0.62, and *Acc* = 0.73 were obtained (Table 4). No significant differences with respect to the case without feature selection were found,

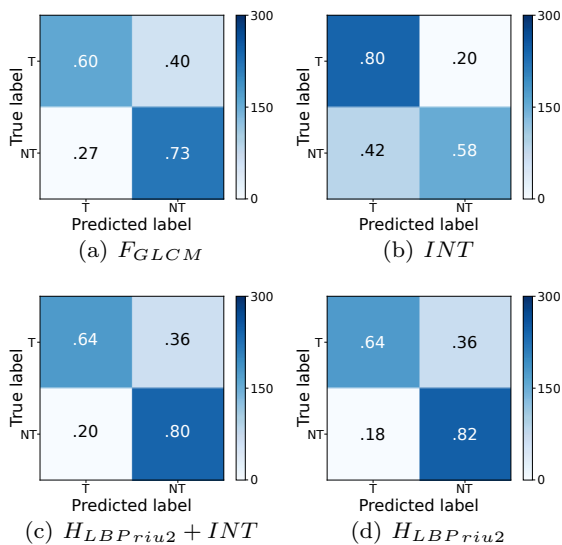


**Fig. 7** Confusion matrices (CMs) for the classification of image patches from transplanted (T) and non-transplanted (NT) liver-graft images. (a) CM for gray-level co-occurrence based-features ( $FGLCM$ ). (b) CM for intensity-based features ( $INT$ ). (c) CM for intensity-based and local binary pattern features ( $H_{LBPriu2} + INT$ ). (d) CM local binary pattern-based features ( $H_{LBPriu2}$ ). CMs were obtained with support vector machines.

**Table 5** Tested feature vectors for semi-supervised image classification with single instance learning - support vector machines and corresponding number of features.  $INT$ : Intensity mean and variance;  $H_{LBPriu2}$ : Normalized histogram of rotation-invariant uniform local binary patterns;  $Blo$ : Blood features.

Feature vector	$H_{LBPriu2} + INT$	$H_{LBPriu2} + INT + Blo$
Number of features	168	177

therefore we decided to avoid using PCA to keep the overall-algorithm computational cost low. Similar results were achieved also with  $H_{LBPriu2} + INT$ .

When classifying  $H_{LBPriu2}$  with RF,  $Se = 0.72$ ,  $Sp = 0.61$ , and  $Acc = 0.67$  were obtained (Table 4). Significant differences with respect to SVM performance were not found.

The visual confusion matrix for the patch classification performed with SVM and  $H_{LBPriu2}$  is shown in Fig. 8.

From our patch-based experimental analysis, among all the tested feature sets,  $H_{LBP} + INT$  and  $H_{LBP}$  were the best-performing feature sets. Thus, we decided to test SVM-SIL with these two feature vectors, including also the  $Blo$  features as introduced in Sec. 2.2.2. The features investigated for SVM-SIL classification and the correspondent number of features are reported in Table 5. With SVM-SIL,  $H_{LBP} + INT + Blo$  showed the best classification performance, with  $Se = 0.95$ ,  $Sp = 0.81$ , and  $Acc = 0.88$ . When using  $H_{LBP} + Blo$ ,

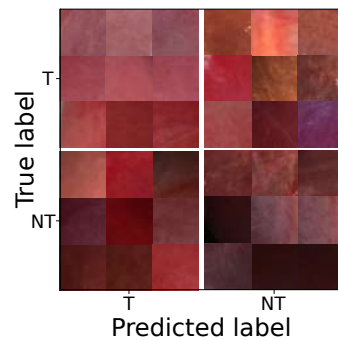


**Fig. 8** Visual confusion matrices for supervised patch classification obtained with the histogram of rotation-invariant uniform local binary patterns and support vector machines. NT: Non-transplanted patches; T = Transplanted patches.

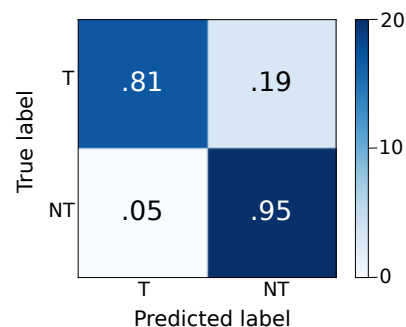


**Fig. 9** Confusion matrix (CM) for the classification of transplanted (T) and non-transplanted (NT) liver-graft images. CM are obtained with  $H_{LBP} + INT + Blo$ . The classification is performed with support vector machines (SVM)-single instance learning (SVM-SIL). The colorbar indicates the number of correctly classified images.

$Acc = 0.82$  was achieved. The confusion matrix for the SVM-SIL classification for  $H_{LBP} + INT + Blo$  is reported in Fig. 9. Visual samples of liver classification outcomes with  $H_{LBPriu2} + INT + Blo$  for SVM-SIL classification are shown in Fig. 10. It is worth noting that SVM-SIL failed in classifying images of rejected liver grafts only once.

As for the algorithm computational cost, the liver manual segmentation took  $\sim 3s$  on average per image. The classification process (both for SVM, RF and SVM-SIL) took  $\sim 10^{-5}s$ . The time for the computation of  $H_{LBP} + INT$  for one patch was  $\sim 0.02s$ . Experiments were performed on a CPU Intel® Core™i7-3537U @ 2.0GHz x 4 with 7.6GB of available RAM; Linux operative system, kernel 4.4.0-98-generic (x86\_64) Ubuntu 16.04.3 LTS distribution.

## 4 Discussion

In this paper, we presented and fully evaluated an innovative approach to the computer-aided assessment of HS in RGB images acquired with smartphones in the



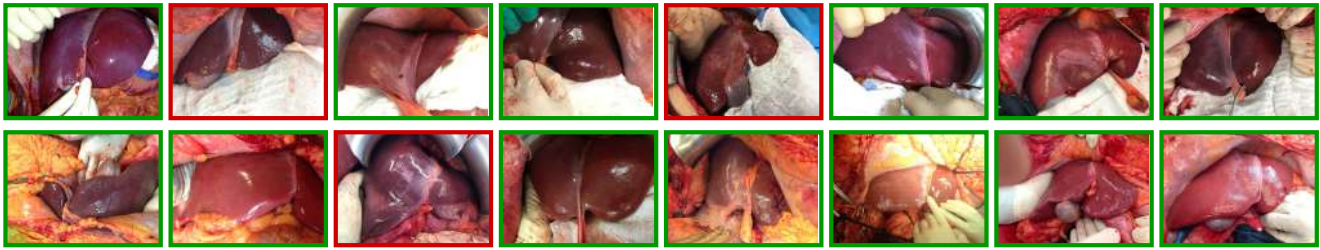


**Fig. 10** Samples of classification outcomes for transplanted (first row) and non-transplanted (second row) liver grafts. Classification refers to support vector machines (SVM) - single instance learning (SIL) with  $H_{LBP_{riu2}} + INT + Blo$ . The green and red boxes refer to correct and wrong classification outcomes, respectively. SVM-SIL wrongly classified a rejected liver only once.

OR, which exploits liver texture analysis coupled with machine learning. With respect to the approaches in the literature, our method only requires RGB images and blood-sample tests. Moreover, it provides the surgeons with a classification outcome on whether to accept or discard a liver graft.

For our experimental analysis, the highest (supervised) patch-classification performance was obtained with  $H_{LBP_{riu2}}$  and  $H_{LBP_{riu2}} + INT$ , which performed equally.  $F_{GLCM}$  performed worse and this is probably due to the GLCM lack of robustness to illumination condition changes. In fact, when acquiring liver images, no assumption on keeping the illumination constant was done, resulting in different levels of illumination in the images. Similarly, also  $INT$  features were not able to face such variability in the illumination.

Classification performance with and without PCA did not differ significantly. Therefore, we decided to avoid performing PCA feature reduction for lowering the algorithm computational cost with a view to real-time applications.

Significant differences were not found when comparing RF and SVM performance. This is something expected, if one compares our results with the literature (e.g. [22, 7]).

By visually inspecting the wrongly classified patches (Fig. 8), it emerged that misclassification occurred for patches that are challenging to classify also for the human eye. In fact, images were acquired without a controlled acquisition protocol, making the classification not trivial.

SVM-SIL provided a more reliable and robust classification with respect to supervised approaches, both in terms of  $Se$  and  $Sp$ . In fact, SVM-SIL misclassified a rejected liver image only once. This can be attributed to the fact that SIL did not make any assumption on ground-truth patch labels, but only exploited the ground-truth classification of the images obtained through histopathology for training purposes. The inclusion of blood-test features helped increasing the clas-

sification accuracy with respect to using only textural features. Nonetheless, it is worth noting that  $Blo$  alone was not sufficient to achieve accurate HS diagnosis. Indeed, during our preliminary analysis, we achieved an  $Acc = 0.75$  with supervised SVM-based classification when considering  $Blo$  alone. This supports the hypothesis that textural-information inclusion is a valid support for HS diagnosis.

The computational time required by the proposed method was not compatible with real-time application due to the computational cost associated with the liver manual segmentation. To reduce the computational cost and make the process more automatic, color thresholding could be used to segment the liver. Nonetheless, in this paper, we decided to perform manual liver masking to keep the experimental setup as controlled as possible with the goal of investigating the potentiality of machine learning in the analyzed context.

A direct comparison with the state of the art results was not possible, due to the lack of benchmark datasets. Moreover, as reported in Sec. 1, the methods in the literature only correlated hepatic physical characteristics with the HS level, not providing a method for graft quality assessment.

A limitation of the proposed study could be seen in its patch-based nature, even though this is something commonly done in the literature for hepatic tissue assessment (e.g. [26]). We decided to work with patches to have a controlled and representative dataset to fairly evaluate different features.

Moreover, due to the size of our dataset, we decided to perform leave-one-patient-out cross validation for the algorithm evaluation. Despite leave-one-patient-out cross validation being a well-established method for performance evaluation based on a small set of samples, it could provide classification-performance overestimation [12]. Therefore, to have a robust estimation of the classification performance, it would be necessary to evaluate the classification method with different sets of images never used for training. Nonetheless, as to do

so, a bigger dataset would be required. Thus, as future work, we aim at enlarging the training dataset, exploiting also different RGB-camera devices, to validate the experimental analysis presented here. We also aim at investigating if including a measure of confidence on classification, such as in [22, 23], could help further improving classification reliability.

## 5 Conclusion

In conclusion, the most significant contribution of this work is showing that LBP-based features and SVM-SIL, along with blood-sample tests, can be used as support for HS assessment. This is highly beneficial for practical uses as the method can be potentially developed to run in real-time, being compatible with the short time available between the time of liver procurement and the LT. Moreover, the only required imaging source is a standard RGB camera, which can be easily used in the OR without requiring additional imaging sources such as MRI or Raman spectrometer.

It is acknowledged that further research is required to further ameliorate the algorithm as to offer all possible support for diagnosis and achieve classification performance comparable with those obtained with biopsy. However, the results presented here are surely a promising step towards a helpful processing system to support the decision process for HS assessment in liver procurement setting.

*Conflict of interest* All authors declare that they have no conflict of interest.

*Ethical standards* All studies have been approved and performed in accordance with ethical standards.

*Informed consent* Informed consent was obtained from all individuals for whom identifying information is included in this article.

## References

- Bhati C, Silva M, Wigmore S, Bramhall S, Mayer D, Buckels J, Neil D, Murphy N, Mirza D (2009) Use of bioelectrical impedance analysis to assess liver steatosis. In: Transplantation Proceedings, Elsevier, vol 41, pp 1677–1681
- Breiman L (2001) Random forests. *Machine learning* 45(1):5–32
- Burges CJ (1998) A tutorial on support vector machines for pattern recognition. *Data Mining and Knowledge Discovery* 2(2):121–167
- Chen CL, Fan ST, Lee SG, Makuuchi M, Tanaka K (2003) Living-donor liver transplantation: 12 years of experience in Asia. *Transplantation* 75(3):S6–S11
- Csurka G, Dance C, Fan L, Willamowski J, Bray C (2004) Visual categorization with bags of keypoints. In: *Workshop on Statistical Learning in Computer Vision, Prague*, vol 1, pp 1–2
- D’alessandro AM, Kalayoglu M, Sollinger HW, Hoffmann RM, Reed A, Knechtle SJ, Pirsch JD, Hafez GR, Lorentzen D, Belzer FO (1991) The predictive value of donor liver biopsies for the development of primary nonfunction after orthotopic liver transplantation. *Transplantation* 51(1):157–163
- Duro DC, Franklin SE, Dubé MG (2012) A comparison of pixel-based and object-based image analysis with selected machine learning algorithms for the classification of agricultural landscapes using SPOT-5 HRG imagery. *Remote Sensing of Environment* 118:259–272
- Esteva A, Kuprel B, Novoa RA, Ko J, Swetter SM, Blau HM, Thrun S (2017) Dermatologist-level classification of skin cancer with deep neural networks. *Nature* 542(7639):115–118
- Goceri E, Shah ZK, Layman R, Jiang X, Gurcan MN (2016) Quantification of liver fat: A comprehensive review. *Computers in Biology and Medicine* 71:174–189
- Haralick RM, Shanmugam K, et al (1973) Textural features for image classification. *IEEE Transactions on Systems, Man, and Cybernetics* 3(6):610–621
- Hewitt KC, Rad JG, McGregor HC, Brouwers E, Sapp H, Short MA, Fashir SB, Zeng H, Alwayn IP (2015) Accurate assessment of liver steatosis in animal models using a high throughput raman fiber optic probe. *Analyst* 140(19):6602–6609
- Kohavi R (1995) A study of cross-validation and bootstrap for accuracy estimation and model selection. In: *Ijcai, Montreal, Canada*, vol 14, pp 1137–1145
- Koneru B, Dikdan G (2002) Hepatic steatosis and liver transplantation current clinical and experimental perspectives. *Transplantation* 73(3):325–330
- Lechaux D, Dupont-Bierre E, Karam G, Corbineau H, Compagnon P, Noury D, Boudjema K (2004) Technique du prélèvement multiorganes: cœur-foie-reins. In: *Annales de Chirurgie*, Elsevier, vol 129, pp 103–113
- Li B, Meng MQH (2009) Texture analysis for ulcer detection in capsule endoscopy images. *Image and Vision Computing* 27(9):1336–1342

16. Liang P, Cong Y, Guan M (2012) A computer-aided lesion diagnose method based on gastroscopel-image. In: Information and Automation, 2012 International Conference on, IEEE, pp 871–875
17. Lin Y, Lv F, Zhu S, Yang M, Cour T, Yu K, Cao L, Huang T (2011) Large-scale image classification: fast feature extraction and SVM training. In: Computer Vision and Pattern Recognition, 2011 IEEE Conference on, IEEE, pp 1689–1696
18. Maier-Hein L, Vedula SS, Speidel S, Navab N, Kikinis R, Park A, Eisenmann M, Feussner H, Forestier G, Giannarou S, et al (2017) Surgical data science for next-generation interventions. *Nature Biomedical Engineering* 1(9):691
19. Mancia C, Loustaud-Ratti V, Carrier P, Naudet F, Bellissant E, Labrousse F, Pichon N (2015) Controlled attenuation parameter and liver stiffness measurements for steatosis assessment in the liver transplant of brain dead donors. *Transplantation* 99(8):1619–1624
20. Marsman WA, Wiesner RH, Rodriguez L, Batts KP, Porayko MK, Hay JE, Gores GJ, Krom RA (1996) Use of fatty donor liver is associated with diminished early patient and graft survival. *Transplantation* 62(9):1246–1251
21. Misawa M, Kudo Se, Mori Y, Takeda K, Maeda Y, Kataoka S, Nakamura H, Kudo T, Wakamura K, Hayashi T, et al (2017) Accuracy of computer-aided diagnosis based on narrow-band imaging endocytoscopy for diagnosing colorectal lesions: comparison with experts. *International Journal of Computer Assisted Radiology and Surgery* pp 1–10
22. Moccia S, De Momi E, Guarnaschelli M, Savazzi M, Laborai A, Guastini L, Peretti G, Mattos LS (2017) Confident texture-based laryngeal tissue classification for early stage diagnosis support. *Journal of Medical Imaging* 4(3):034,502
23. Moccia S, Wirkert SJ, Kenngott H, Vemuri AS, Apitz M, Mayer B, De Momi E, Mattos LS, Maier-Hein L (2018) Uncertainty-aware organ classification for surgical data science applications in laparoscopy. *IEEE Transactions on Biomedical Engineering*
24. Mor E, Klintmalm GB, Gonwa TA, Solomon H, Holman MJ, Gibbs JF, Watemberg I, Goldstein RM, Husberg BS (1992) The use of marginal donors for liver transplantation. a retrospective study of 365 liver donors. *Transplantation* 53(2):383–386
25. Ojala T, Pietikainen M, Maenpaa T (2002) Multiresolution gray-scale and rotation invariant texture classification with local binary patterns. *IEEE Transactions on Pattern Analysis and Machine Intelligence* 24(7):971–987
26. Qayyum A, Nystrom M, Noworolski SM, Chu P, Mohanty A, Merriman R (2012) MRI steatosis grading: development and initial validation of a color mapping system. *American Journal of Roentgenology* 198(3):582–588
27. Quéllec G, Cazuguel G, Cochener B, Lamard M (2017) Multiple-instance learning for medical image and video analysis. *IEEE Reviews in Biomedical Engineering*
28. Rogier J, Rouillet S, Cornélis F, Biais M, Quinart A, Revel P, Bioulac-Sage P, Le Bail B (2015) Noninvasive assessment of macrovesicular liver steatosis in cadaveric donors based on computed tomography liver-to-spleen attenuation ratio. *Liver Transplantation* 21(5):690–695
29. Selzner M, Clavien PA (2001) Fatty liver in liver transplantation and surgery. In: *Seminars in Liver Disease*, Copyright© 2001 by Thieme Medical Publishers, Inc., 333 Seventh Avenue, New York, NY 10001, USA. Tel.:+ 1 (212) 584-4662, vol 21, pp 105–114
30. Shen X, Sun K, Zhang S, Cheng S (2012) Lesion detection of electronic gastroscopel images based on multiscale texture feature. In: *Signal Processing, Communication and Computing (ICSPCC)*, 2012 IEEE International Conference on, IEEE, pp 756–759
31. Yersiz H, Lee C, Kaldas FM, Hong JC, Rana A, Schnickel GT, Wertheim JA, Zarrinpar A, Agopian VG, Gornbein J, et al (2013) Assessment of hepatic steatosis by transplant surgeon and expert pathologist: A prospective, double-blind evaluation of 201 donor livers. *Liver Transplantation* 19(4):437–449
32. Zhang Y, Wirkert SJ, Iszatt J, Kenngott H, Wagner M, Mayer B, Stock C, Clancy NT, Elson DS, Maier-Hein L (2017) Tissue classification for laparoscopic image understanding based on multispectral texture analysis. *Journal of Medical Imaging* 4(1):015,001–015,001